Plasma Sources
Science and
Technology

PAPER • OPEN ACCESS

Plasma-substrate interaction in a dual frequency APPJ

To cite this article: Alessandro Patelli *et al* 2025 *Plasma Sources Sci. Technol.* **34** 025010

View the article online for updates and enhancements.

You may also like

- Collision integrals of electronically excited atoms in air plasmas: II. N–O interactions
Wensheng Zhao, Qizhen Hong, Chao Yang et al.

- A deep learning approach for electric field profile reconstruction based on the E-FISH method
Zhijian Yang, Edwin Setiadi Sugeng and Tat Loon Chng

- Computational study of characteristics of atmospheric pressure glow discharge in helium
Gubad Islamov, Ender Eylenceoglu and Ismail Rafatov

HIDEN ANALYTICAL
Analysis Solutions for your Plasma Research
For Surface Science
Surface Analysis
SIMS
3D depth Profiling
Nanometre depth resolution
Compact SIMS
SIMS Workstation
Auto SIMS
For Plasma Diagnostics
Plasma characterisation
Customised systems to suit plasma Configuration
Mass and energy analysis of plasma ions
Characterisation of neutrals and radicals
ESPion
HPR-60 MBMS
EQP Series
Click to view our product catalogue
Knowledge
Experience
Expertise
Contact Hiden Analytical for further details:
www.HidenAnalytical.com
info@hiden.co.uk

This content was downloaded from IP address 193.206.156.92 on 12/03/2025 at 15:58

OPEN ACCESS
IOP Publishing

Plasma Sources Science and Technology

Plasma Sources Sci. Technol. **34** (2025) 025010 (19pp)

https://doi.org/10.1088/1361-6595/adb514

Plasma-substrate interaction in a dual frequency APPJ

Alessandro Patelli[1,*], **Silvia Giuditta Scaltriti**[2], **Arturo Popoli**[2], **Emilio Martines**[3] **and Andrea Cristofolini**[2]

[1] Department of Physics and Astronomy 'Galileo Galilei', University of Padova, via Marzolo 8, Padova 35131, Italy
[2] Department of Electrical, Electronic, and Information Engineering 'Guglielmo Marconi', University of Bologna, viale Risorgimento 2, Bologna 40136, Italy
[3] Department of Physics 'G. Occhialini', University of Milano-Bicocca, piazza della Scienza 3, Milano 20126, Italy

E-mail: alessandro.patelli@unipd.it, silvia.scaltriti2@unibo.it, arturo.popoli@unibo.it, emilio.martines@unimib.it and andrea.cristofolini@unibo.it

Received 3 April 2024, revised 25 December 2024
Accepted for publication 12 February 2025
Published 20 February 2025

Abstract

To achieve a uniform argon plasma in an atmospheric pressure jet, we explored the possibility of using dual-frequency excitation in a coaxial dielectric barrier discharge device. Two separate ring-shaped electrodes outside an alumina tube generate the two frequencies. The upstream electrode is powered at low frequency (LF, 17 kHz), while the downstream electrode is powered at radio frequency (RF, 27 MHz). To assess the interaction with the substrate, a grounded electrode, covered by a glass substrate, is placed 5 mm from the outlet of the alumina tube. We analyze the device with a fluid model and compare the results with experimental electrical and optical characterization. As the plasma is ignited by the LF, positive streamers develop from the LF electrode and reach the substrate in a few hundred nanoseconds. At this stage, the substrate is charged and a surface discharge propagates on the glass; however, no additional ionization occurs in the jet. As RF is added, the plasma is sustained by modulation in the Ω regime. At the same time, the LF polarization propagates through the plasma, influencing the sheaths on the facing dielectric walls. When the voltage drop in the sheaths exceeds a threshold level, an additional γ mode originates due to the secondary electrons emitted by the surfaces, leading to an increase in power dissipation. This coexistence of the two regimes is observed in the simulation, and it is validated experimentally by time-resolved photoemission measurements. As a result, the dual-frequency plasma exhibits a filamentary structure similar to that of an LF-driven jet. However, RF excitation caused diffused pre-ionization of the gas, which reduced the charge density gradients, resulting in wider microdischarge channels and a lower average electric field. Streamers propagation is therefore limited, while an ion flow to the substrate is maintained and controlled by the LF polarization.

Supplementary material for this article is available online

Keywords: APPJ, simulation, dielectric barrier discharge, dual frequency, RF hybrid regime, diffuse DBD

[*] Author to whom any correspondence should be addressed.

Original Content from this work may be used under the terms of the Creative Commons Attribution 4.0 licence. Any further distribution of this work must maintain attribution to the author(s) and the title of the work, journal citation and DOI.

© 2025 The Author(s). Published by IOP Publishing Ltd

1. Introduction

The prospect of achieving a diffused plasma in a glow regime under atmospheric pressure conditions has consistently drawn the attention of researchers. This interest comes from the goal of improving the reproducibility of processes and of facilitating control over temperature, density, and charge flux [1, 2]. Nevertheless, plasma propagation at atmospheric pressure poses challenges as a result of a highly collisional regime, which accelerates and localizes energy exchanges. Consequently, propagation is typically guided by fluctuations, particularly thermal instabilities [3]. In this scenario, increases in the confined electron density result in gas heating, leading to a rise in the reduced field, which, in turn, triggers a positive feedback mechanism on density. These instabilities are responsible for the filament-like behavior of plasma propagation, the unpredictable movement of plasma channels, and their branching leading to the arc transition.

Historically, this transition was avoided by employing dielectric layers and capacitive or resistive ballasts. Nevertheless, these techniques mainly limit the flow of current within plasma channels without impacting the formation process. One method of addressing the ignition, achieving a diffused plasma, is to reduce the electric field required for ionization processes. An example is offered by the Townsend regime, where the electric field is below the threshold required for ionization amplification [4], as dictated by the Meek criterion. However, this involves compromising the plasma density, and additionally, the volume of plasma becomes confined between the electrodes. This does not meet the criteria for a plasma jet developing outside the nozzle.

A different approach that specifically targets the thermal instability is to improve energy transfer, for instance, by utilizing helium, which is known for its high mobility. Furthermore, particular circumstances may also facilitate an enhancement in charge diffusion, such as when the mass gas velocity and the ion drift are comparable [5]. In any case, the most commonly employed strategy is based on the use of Penning mixtures, in which the energy stored in metastable states diffuses in the plasma unaffected by the electric field [6, 7]. Gas combinations such as helium-nitrogen (He-N_2) or argon-ammonia (Ar-NH_3) enable the generation of glowing dielectric barrier discharges (DBD) over a broad spectrum of frequencies [1].

Since localized heating and thermalization are time-dependent processes, the self-propagating regime can also be stabilized by the use of rapidly changing electric fields. In the case of nanopulsed high-voltage devices, the plasma propagates as a bullet (an advancing space charge), creating an intense self- electric field, which allows electrons to reach high temperatures [8]. However, this configuration is not suitable for high-power density applications.

This requirement is usually satisfied by the use of radio frequency (RF) devices. At megahertz frequencies (RF), the field oscillation period is comparable to the propagation time of streamers. In this regime, the ion drift is significantly reduced, while electrons can still respond to the field oscillations, enabling effective heating. At low pressure collisions are reduced, so electrons can freely move to shield the electric field in the bulk of the plasma. As a consequence, electron heating is confined within the oscillating sheaths; this regime is called the α-mode. At high pressure, reduced electron mobility prevents efficient shielding of the electric field within the plasma bulk, allowing the field to penetrate deeper and drive heating currents throughout the plasma. This bulk heating mechanism is primarily resistive, as the energy is dissipated through collisions between electrons and neutrals, and is therefore termed the Ω mode [9]. Regardless of pressure, electrons are heated during both the expansion and contraction of the sheaths during an RF cycle; the modulation of the ionization process is twice the RF frequency. In RF devices, dielectric barriers can be removed, enabling better power dissipation and achieving larger plasma densities. However, the gas temperature increases as a result of Joule heating caused by collisions between bulk electrons and neutrals, whereas the electron temperature remains relatively low because of relatively weak electric fields.

As the RF power increases, the voltage drop in the sheaths also increases, and the secondary electrons emitted by the walls are accelerated towards the plasma bulk. Therefore, these secondary electrons act as an additional ionization source. At low pressure, these electrons can gain enough energy to directly ionize the neutral gas and lead to the so-called γ mode. At atmospheric pressure, the energy gain is lower due to frequent collisions; however, it is sufficient to directly ionize the gas [10] or more easily excite metastable states, which can lead to ionization through the Penning process [11]. As the ionization process is enhanced with increasing power levels, the electron temperature remains low. Therefore, to improve the nonthermal character of plasma at atmospheric pressure, structured electrodes [12] or dual frequency setups [13–15] are suggested in the literature. The first solution achieves electric field enhancements by introducing sharp angles or holes in the electrode geometry. In the latter, a constructive interference effect is often exploited by using a combination of frequencies in the RF band. Both approaches increase the electron temperature while maintaining a diffused plasma. However, when used in a jet configuration, the plasma is confined between the electrodes, and the charge flow to the substrate is limited.

On the other hand, significant ion fluxes to a substrate can be achieved in a dual frequency parallel plate configuration by combining kilohertz (LF) and megahertz (RF) excitations [16]. This coupling has been investigated both experimentally and by 1D modeling [11, 17, 18]. As a result of the coupling, the RF plasma exhibits a hybrid mode with a transition from the Ω to the γ-mode depending on the relative polarization of the electrodes. In another perspective, the LF voltage induces an ions drift to the cathode, reducing the plasma density in the bulk. In this condition, the Ω excitation is reduced in the bulk and to the anode. Currently, on the cathode side, alternatively adding or subtracting the RF voltage, a pulsed emission of the secondary electrode occurs and, consequently, triggers the γ excitation when both polarizations are negative. Therefore, there is a competition between the RF parameters, which control plasma creation in the discharge bulk, and the LF voltage, which controls the drift of ions, that is, their losses [18]. At the

same time, ignition of the γ-mode is gated by satisfying a self-sustainment criterion and an essential role is identified in the photons emitted by the excimer Ar_2^*, which enhance secondary electron emissions [19].

Dual-frequency RF + LF have also been considered to produce plasma jets [16, 18, 20]. This configuration appeared to lead to interesting results in several applications, from the restoration of cultural heritage [21] to surface doping [22], treatment in liquids [23] or functionalization of scaffolds for tissue engineering [24, 25]. In a dual-frequency device, the two waveforms are applied in different regions of the jet and, as suggested in the literature [16] and probably depending on the distance, it can be assumed that two spatially separated discharges are generated. However, in this work, we show that in the coaxial geometry of an atmospheric pressure plasma jet (APPJ), the simultaneous excitation with different electrodes supplied with different frequencies generates a single plasma volume, which, in turn, couples the electrodes. In addition, that coupling is also transferred to the substrate, through the same plasma. To provide this information, a 2D simulation of a coaxial APPJ with a distance between electrodes greater than 1 cm was set up. Electrical and optical characterization was performed close to the substrate at the outlet of the jet to validate the simulation findings and better understand the behavior of the discharge.

2. Method

2.1. The experimental setup

The APPJ device used for the model and its experimental validation was based on Plasma Stylus Noble (Nadir srl) [26], which already implements dual frequency generation. However, in our custom experimental setup, the design was simplified by removing nozzles at the outlet. The device, shown in figure 1, was designed with a coaxial configuration with two excitation-ring electrodes positioned outside an alumina tube. The tube had a diameter of 9 mm and a wall thickness of 0.5 mm. The spacing between the two high-frequency (LF) electrodes upstream was 2 mm, with the one downstream grounded. A radio frequency electrode (RF) was placed 13 mm downstream, 3 mm from the jet outlet. A glass substrate was placed 5 mm below the end of the tube. The argon flux in the tube was kept at 5.0 slm using a Bronkhorst Mass-View controller.

In the model, the environmental gas was assumed to be pure argon, whereas during the experimental observation the gas flows to the open air without any confinement. Since the distance between the jet outlet and the substrate was 5 mm, from previous studies [27, 28] it can be expected that the air concentration in the plasma region on the glass surface could be around 1-2%. However, during propagation in open air, the plasma moves through argon channels, where the concentration of the noble gas is higher [29]. In our case the flow has a speed of about 5 $\mathrm{m\,s^{-1}}$ and considering the geometry, the Reynolds number is below 500, indicating laminar flow conditions. A potential transition to turbulent flow can be triggered by the plasma ignition and to the associated localized

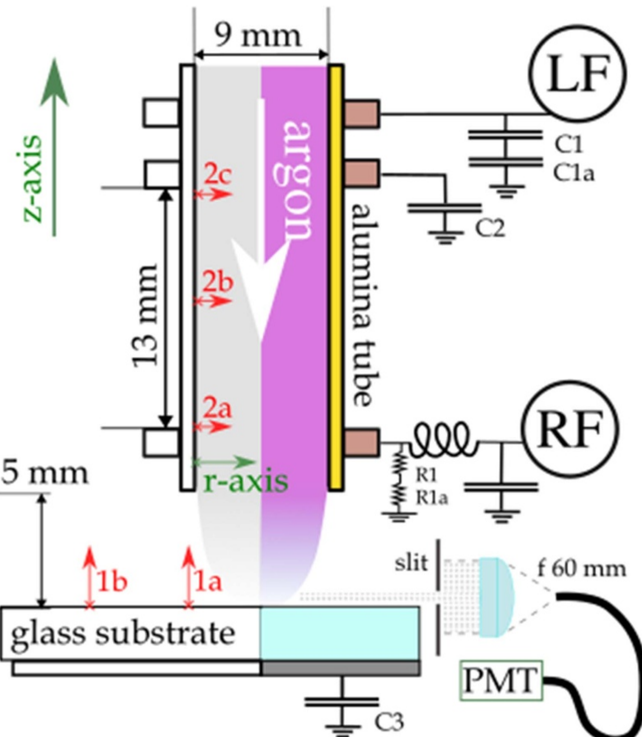

Figure 1. Scheme of the dual frequency APPJ. Argon flows through an alumina tube, with a microscope glass slide positioned in front of the outlet. Ring-shaped electrodes are placed externally around the tube. Upstream, a low-frequency (LF) electrode and a ground electrode are positioned, while a radio-frequency (RF) electrode is located downstream. A resistor $R1$ and capacitive $C1$ divider are used to measure the electrodes voltages, while $C2$ and $C3$ to measure the charge collected to ground through the substrate and the ring along the tube. The optical emission, temporally resolved, is obtained by collecting the parallel light passing through horizontal slits positioned at 1 cm from the jet and detected by a photon multiplier tube (PMT). On the left grayscale side of the scheme, the positions where simulation data are used to discuss the discharge behavior in the article are highlighted in red: $1a, b$ refer to substrate interaction figure 6 and $2a, b, c$ to the coupling mechanism between the electrodes figure 9.

heating, because electrohydrodynamic forces are negligible in argon. However, as can be observed from the ICCD images in figure 4, plasma propagation follows laminar flow lines, indicating that no Kelvin–Helmholtz instabilities were activated. Under these laminar flow conditions, the plasma propagation regime is not affected within the laminar flow channel, and the argon metastables remain within the channel, which is also where streamers develop [29]. We therefore expect that the model can overestimate the density of electrons and argon metastables in the outer regions, but this should not significantly affect the overall qualitative description of the propagation mechanism, particularly in the regions characterized by laminar flow.

The LF generator was a Nadir high voltage power supply up to 15 kV, with sinusoidal waveform and frequency regulation from 15 to 21 kHz. During the experiments, the frequency was manually set to 17 kHz to optimize the power transfer. The RF power supply was a SEREN R301 that worked at

27.12 MHz and the plasma impedance was matched by an LC network specifically designed. The electrode and the matching box were connected by a 15 cm long RG174 coaxial cable. An aluminum tape, grounded and wider than the area where the plasma touches the glass, was positioned beneath the microscope slide, which serves as the soda-lime glass substrate.

The LF voltage was recorded through a capacitive divider $C1$ with five RF High-voltage barrel capacitors $C1$ 122 pF (High Energy Corp. HT50) in series and a last ceramic capacitor to ground $C1a$ of 4.7 nF (Vishay 615R series). The voltage was measured with a voltage probe in $C1a$ (Tektronix TPP1000, 1 GHz bandwidth). All electric signals were acquired by a Tektronix MSO44 oscilloscope (1 GHz bandwidth). The RF voltage was monitored using a resistive divider $R1$ (Vishay / Techno CRHA high voltage thick film chip resistors) placed between the RF electrode and the LC network. The resistive divider was calibrated at the working frequency of 27 MHz by applying voltages of up to 2 kV to the RF electrode. The voltage was read across $R1a$ connecting directly to the oscilloscope (impedance 1 Ω) in parallel. To estimate the charges on the glass surface, an aluminum tape was connected to ground by a series capacitor $C3 = 22$ pF (Vishay 564R series). The charge collected on $C3$ was measured with a voltage probe (Tektronix TPP1000, 1 GHz bandwidth). The charge collected on the ground ring of the LF discharge around the alumina tube was recorded by voltage measurements on a series capacitor $C2$ of 680 pF (Vishay 564R series).

Light emission was captured using a converging lens with a 60 mm focal length, aligned perpendicularly to the jet flow. A 2 m long optical fiber with a 400 μm core was placed at the focal point of the lens to collect light from the collimated beam. To delineate the volume of plasma under investigation, a horizontal slit parallel to the glass surface 1 cm was placed away from the jet. The slit was 200 μm in height and 1 cm wide and was placed 500 μm above the glass surface. The fiber was connected with a Hamamatsu E5576 fiber adapter to a photomultiplier tube (Hamamatsu PMT H11901-20). The PMT was managed by the power supply C7169, the control voltage was set to 1 V. The PMT signal output was directly connected to the Tektronix MSO44 oscilloscope (1 GHz bandwidth). The recorded signal is shown in figure S6, the sampling was set at 3.125 GS/s, the intrinsic rise time of the PMT is 0.57 ns and the resulting width of the PMT signals is about 1.6 ns, which is in agreement with the oscilloscope bandwidth. The slit was adjusted to a height that enabled the collection of ample statistical data while ensuring that the detection signals from different photons did not overlap. As shown in figure S6, peaks corresponding to single-photon detection events were counted and associated with the other electrical signals for histogram construction. Spectrally, no corrections were made to take into account the PMT spectral sensitivity and fiber optical transmission. The number of photons derived, therefore, is not an absolute measurement but the number of photons detected by the PMT.

The oscilloscope, in combination with a RIGOL DG2072 arbitrary function generator, was also used to trigger a gated camera (PSEL ICMOS Photonic Science) to visualize plasma propagation.

2.2. The fluid model

The simulation work was carried out using laminar flow and plasma modules in COMSOL 6.0. The geometry included a 3 cm long tube and a 2 cm wide substrate 5 mm away from each other. Taking into account the total volume and length of the surfaces in contact with the plasma, which required a mesh of about 3 μm, the model required several approximations.

First, the gas flow and plasma evolution were solved separately under stationary conditions and in the time domain, respectively. The time evolution of the plasma was simulated for a 60 μs long time interval starting from the LF discharge ignition. Taking into account a gas flow of 5 slm in a tube of diameter 9 mm, the gas speed would be on the order of 5 m s^{-1}. Despite the fact that the plasma gas heating may cause the velocity to increase twofold [30], the maximum movement of the gas species caused by the flow during the simulation remains at 0.6 mm. Thus, the effect of the fluid dynamics is considerably smaller compared to the geometrical dimensions of the model on that short time scale. This suggests that, as an initial approximation, the effect of gas heating can be disregarded. In addition, although the stationary solution of the bulk speed of gas can also contribute to the spatial distribution of plasma and vortex formation, its influence on discharge frequency coupling was deemed negligible in this study. This approximation simplified the calculations, avoiding iteration between the different physics modules. Anyway, the plasma evolution was solved by taking into account the stationary velocity and pressure fields obtained in the fluid dynamic module.

To further reduce the calculation time, a 2D axially symmetric geometry was considered; therefore, a full description of the filamentary structure of the plasma could not be resolved. However, with respect to the 1D models used to study parallel plate configurations, the 2D models offer the ability to consider the spatial arrangement of different electrodes relative to the plasma volume, in particular the LF, the RF, and the substrate.

2.2.1. Fluid dynamic module.

As the flow model was resolved separately from the plasma, energy conservation was not taken into account. Since the model starts in a plasma-off condition and then simulates ignition for few tens of microseconds, we selected from the literature a background temperature for the argon gas of 450 K. This temperature is consistent with an off-period of discharge in an RF APPJ in pulsed mode [30]. To reach thermal equilibrium by plasma heating, it would require a longer time than 60 μs considered in the simulation. However, as the plasma is ignited, the gas temperature certainly increases. A typical spectrum of the OH band (A-X) is shown in figure S3 and shows rotational temperature in the dual frequency mode on the order of 620 K, which sets an upper limit on the temperature increase. The main source of gas heating is the RF power. In figure S5 the thermal load on a copper plate is presented as a function of the RF power and distance. The results clearly highlight the dependence on the RF power, whereas the influence of distance is negligible. In any case, in our model approximation, since we do not

take into account the gas heating by the plasma, a change in the gas temperature used in the fluid dynamic model only affects the overall gas density. Therefore, we considered these changes in equilibrium temperature negligible relative to the other approximations made.

The flow was then found as a function of the velocity $\mathbf{u}$ of the gas, solving the continuity and Navier–Stokes equations for incompressible fluids

$$\rho\nabla\cdot\mathbf{u}=0 \tag{1}$$

$$\rho(\mathbf{u}\cdot\nabla)\mathbf{u}=-\nabla p+\nabla\cdot\left[\mu\left(\nabla\mathbf{u}+(\nabla\mathbf{u})^T\right)-\frac{2}{3}\mu(\nabla\cdot\mathbf{u})\mathbf{I}\right] \tag{2}$$

where p is the pressure and μ the dynamic viscosity, which is the only parameter dependent on the gas temperature in our case. A no-slip boundary condition was enforced at the walls and on the substrate surface. The velocity and density of the gas was assigned at the glass tube inlet, and a recirculation boundary condition was assigned at the open boundaries downstream of the tube tip. The results of the simulation are shown in the Supplementary Material (figure S1). The resulting flow is compatible with the laminar assumption with a Reynolds number less than 500 and a maximum compression coefficient of about 0.01. The maximum speed resulted in approximately $5\,\mathrm{m\,s^{-1}}$ in the middle of the alumina tube, which is on average lower than in other experiments found in the literature due to the wider diameter of the tube.

2.2.2. Plasma module. The plasma fluid model was based on a simplified reaction kinetic model to reduce the computation time. The model considered electrons, atomic (Ar^+) and molecular (Ar_2^+) ions, as well as excited states (Ar^*), which were treated as a single compound state, grouping the resonant and metastable states of the 4 s system. Since the energy of metastable and resonant states is very close, there is a high probability that a metastable will transition into a resonant and a resonant will transform into a metastable by electron collisions [19]. Therefore, we assumed that they are in Boltzmann equilibrium with the electron temperature and assigned to the compound state an average decay frequency. We do not expect that this simplification compared to more comprehensive reaction schemes [44], where resonant ($1s_2$ and $1s_4$) and metastable states ($1s_3$ and $1s_5$) are treated separately, would affect the description of discharge evolution. In addition, we avoided including the lumped higher states ($2p_{10...5}$ and $2p_{4...1}$) since their density is lower than that of 4 s [45]. On the other hand, we preferred to include the molecular excited states of argon $Ar_2\,(1\Sigma_u^+)$ and $Ar_2\,(3\Sigma_u^+)$ that are known to strongly affect discharge at atmospheric pressure [46]. In addition, through reactions 7 and 8, which require low-energy electron impact, they are a major source of Ar_2^+ ions [45].

At first, a 0D model was run to obtain the rates of the electron impact reactions and electron transport coefficients by solving the 0D Boltzmann two-term equation for electrons, considering electron-electron interactions as functions of the reduced electric field and degree of ionization. The computed EEDF depends on the fraction of each species considered in the gas mixture ($Ar, Ar^*, Ar_2\,(1\Sigma_u^+), Ar_2\,(3\Sigma_u^+)$). However, since the addition of three other parameters would affect the computational burden in the 2D model, to provide a qualitatively accurate estimate of the mixture, we performed a simulation of the 2D problem limited to a LF-only discharge, assuming a Druyvesteyn EEDF and all reactions included in table 1. The density of the molecular species was then evaluated in three different stages of discharge close to the cathode and the anode as a function of the distance from the alumina tube wall (figure S2). Based on the results obtained in the domain region with the highest electron density n_e, metastable Ar and molecular species were expressed as $Ar^*=5\cdot n_e, A_2(1\Sigma_u^+)=10^{-1}\cdot Ar^*, Ar_2(3\Sigma_u^+)=10\cdot Ar^*$. These ratios were then used to determine the input mass fraction for the Boltzmann solver. As an output result, we obtained the lookup tables of the rates of electron impact reactions (1-2,5-8,13) and electron transport coefficients, which are indicated in the table 1 as a function, in fact, of the mean electron energy and density $f(\bar{\epsilon},n_e)$.

Later, we considered the 2D model with rotational axial symmetry based on the jet geometry design (figure 1) that included all the reaction kinetics considered in table 1. In this case, the model was solved in the time domain without constraints in species relative densities and using the lookup tables obtained in the 0D model for electron impact reaction rates and transport coefficients. The 2D fluid model was solved using COMSOL 6.0 under the local mean energy approximation. The governing equations for electrons are as follows:

$$\frac{\partial n_e}{\partial t}+\nabla\cdot\mathbf{\Gamma}_{\boldsymbol{e}}=R_e-(\mathbf{u}\cdot\nabla)n_e \tag{3}$$

where the electron flux $\mathbf{\Gamma}_{\boldsymbol{e}}$ in the drift diffusion approximation and neglecting thermal diffusion can be expressed as

$$\mathbf{\Gamma}_{\boldsymbol{e}}=-(\mu_e\cdot\mathbf{E})n_e-D_e\nabla n_e. \tag{4}$$

As previously presented, electron mobility μ_e and diffusivity D_e were obtained as a solution of the 0D Boltzmann equations. The generation rate R_e of electrons was determined using the complete set of reactions, including the electrons in table 1. The laminar flow solution is included in the equation due to the neutral fluid velocity vector $\mathbf{u}$. The electron density n_e is solved coupled to the electron energy density $n_\epsilon=n_e\bar{\epsilon}$ following the equations

$$\frac{\partial n_\epsilon}{\partial t}+\nabla\cdot\mathbf{\Gamma}_{\boldsymbol{\epsilon}}=S_{en}-(\mathbf{u}\cdot\nabla)n_\epsilon \tag{5}$$

$$\mathbf{\Gamma}_{\boldsymbol{\epsilon}}=-(\mu_\epsilon\cdot\mathbf{E})n_\epsilon-D_\epsilon\nabla n_\epsilon. \tag{6}$$

Electron energy mobility μ_ϵ and diffusivity D_ϵ were also obtained by solving the 0D Boltzmann equation for electrons. The electron energy loss S_{en} was calculated considering the contribution of the different inelastic collisions as presented in table 1. The densities of all other species considered were obtained by solving the respective equations (3) and (4). The electrical mobility of the ions was calculated as a function of

Table 1. Reactions included in the plasma model. The dimensions of the rate coefficients are ($m^3 s^{-1}$) for two-body reactions, ($m^6 s^{-1}$) for three-body-reactions and (s^{-1}) for radiation processes. The electron temperature $T_e = 2\bar{\epsilon}/(3k_B)$ is specified in (K), and the heavy particle temperature in our model is fixed at $T_g = 450$ K.

No.	Reaction	Rate coefficient	ΔE (eV)	References
	elastic			
1	$e + Ar \rightarrow e + Ar$	$f(\bar{\epsilon}, n_e)$	–	[31]
	excitation			
2	$e + Ar \rightarrow e + Ar^*$	$f(\bar{\epsilon}, n_e)$	11.5	[32, 33]
3	$Ar^* + 2Ar \rightarrow Ar_2^{*1} + Ar$	$k = 2.5 \cdot 10^{-44}$	–	[34]
4	$Ar^* + 2Ar \rightarrow Ar_2^{*3} + Ar$	$k = 8.3 \cdot 10^{-45}$	–	[34]
	electron impact ionization			
5	$e + Ar^* \rightarrow 2e + Ar^+$	$f(\bar{\epsilon}, n_e)$	4.427	[31]
6	$e + Ar \rightarrow 2e + Ar^+$	$f(\bar{\epsilon}, n_e)$	15.8	[35]
7	$e + Ar_2^{*1} \rightarrow 2e + Ar_2^+$	$f(\bar{\epsilon}, n_e)$	3.15	[36]
8	$e + Ar_2^{*3} \rightarrow 2e + Ar_2^+$	$f(\bar{\epsilon}, n_e)$	3.23	[36]
9	$Ar + Ar + Ar^+ \rightarrow Ar_2^+ + Ar$	$k = 2.25 \cdot 10^{-43} \cdot \left(\frac{300}{T_g}\right)^{0.4}$	–	[37]
	associative ionization			
10	$Ar^* + Ar^* \rightarrow e + Ar + Ar^+$	$k = 5.60 \cdot 10^{-16}$	–	[38]
	recombination			
11	$e + Ar_2^+ \rightarrow Ar^* + Ar$	$k = 8.1 \cdot 10^{-13} \cdot \left(\frac{300}{T_e}\right)^{0.64} \left(\frac{300}{T_g}\right)^{0.86}$	−2.5	[39]
12	$e + Ar + Ar^+ \rightarrow Ar + Ar$	$k = 1.0 \cdot 10^{-37}$	–	[40]
	de-excitation			
13	$e + Ar^* \rightarrow e + Ar$	$f(\bar{\epsilon}, n_e)$	−11.5	[32, 33]
	quenching			
14	$Ar^* + Ar \rightarrow Ar + Ar$	$k = 3.0 \cdot 10^{-21}$	–	[41]
15	$Ar^* \rightarrow Ar$	$k = 2.01 \cdot 10^6$	–	[42, 43]
16	$Ar_2^{*3} \rightarrow 2Ar$	$k = 3.13 \cdot 10^5$	–	[42, 43]
17	$Ar_2^{*1} \rightarrow 2Ar$	$k = 2.38 \cdot 10^8$	–	[42, 43]

the reduced electric field [47–49], while the diffusion coefficient for all heavy species was set at $1.0 \cdot 10^{-4}\,m^2/s$. The electric field was obtained from the electrostatic potential, which, in turn, was computed by solving a Poisson problem.

The boundary conditions of equations (3)–(6) were established taking into account the axial rotational symmetry along the axis of the alumina tube and the surface charge of the dielectric surfaces. A zero flux boundary condition was enforced for the electrons at the inlet and outlet of the domain, while the flux to the dielectrics was modeled with a reflection coefficient of 0.3 [45]. The thermal emission of electrons from the surfaces was not included. The secondary emission coefficient due to the flux of charged species onto the walls was set to $\gamma_e = 0.02$, following previous works in the literature involving dielectric surfaces [45]. When hitting a wall, heavy species neutralize and de-excite to the ground state. For the Poisson equation, the boundary conditions were consistent with the LF and RF supply voltages at the electrodes and with the ground potential at the downstream LF electrode and beneath the substrate. The relative permittivities considered for the tube alumina and the substrate silica slide were 10 and 3.75, respectively.

The simulations were started with a Gaussian seed charge with a peak value of the order of $4.0 \cdot 10^{17}\,m^{-3}$ of electrons, maintaining and constraining electroneutrality using argon ions. The seed charge was placed 1mm away from the wall of the alumina tube and 4mm from its outlet. Two different simulations were run, with and without RF. The LF voltage was set with a frequency of 17 kHz and a maximum voltage of 5 kV. In the case of coupled electrodes, the LF voltage was turned on after running 41.5 μs of the only RF, which corresponds to more than 1000 cycles. This measure was taken as a precaution to accelerate the computation time by applying the voltage supply sequentially, but it proved to be unnecessary. In the article, the time line for the RF+LF configuration was changed to facilitate comparison with the LF-only case; therefore, 0 μs refers to activation of the LF electrode. Both cases were solved using adaptive triangular grids constituted by up to 225 000 triangular elements. The regions near the walls were discretized as boundary layers, and the plasma in contact with the dielectric walls required a mesh resolution of about 2.5 μm.

3. Results

To better highlight the differences between a dual frequency discharge and a streamer discharge, the model was run with and without RF. This approach allowed us to investigate how the discharge is affected by RF insertion under equal approximations. In addition, the LF-only simulation allowed us to benchmark the model against a standard LF DBD streamer

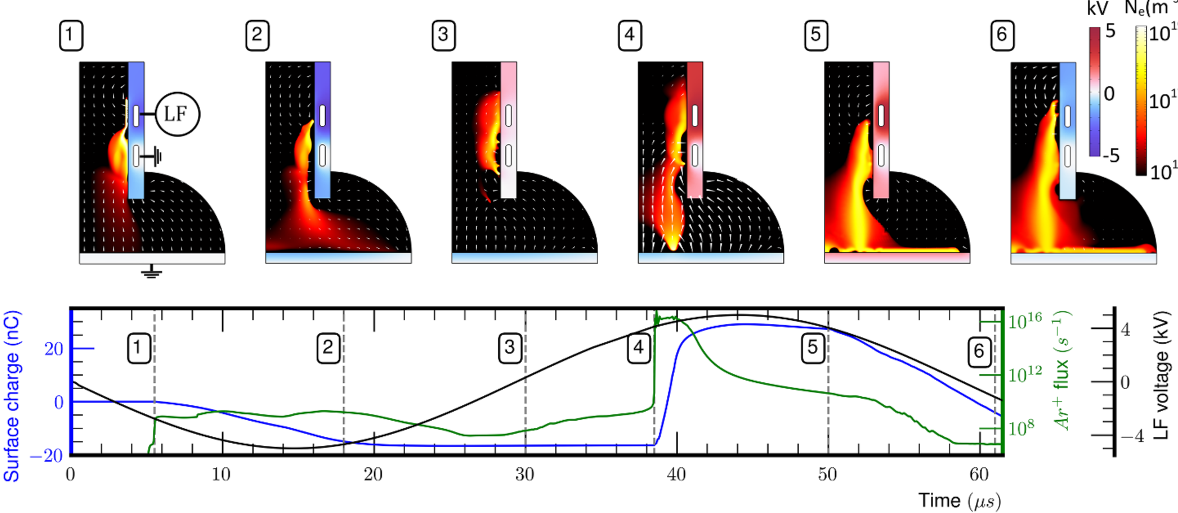

Figure 2. Results of the simulation of the LF-only discharge in argon. (*bottom*) In the graph are reported as a function of time the surface charge and the Ar^+ flux integrated over the entire surface of the glass substrate, and the LF electrode voltage. (*top*) Six critical events are identified, and the respective simulation snapshots of the electron density and electric fields vectors together with voltages in the dielectrics are illustrated.

discharge. The results of the simulation of discharge evolution, with and without RF, are shown in figures 2 and 3 over an LF cycle. In the model with LF-only, the RF electrode was removed while the LF electrodes were placed close to the outlet. This geometry change was required because if the LF electrodes were not shifted closer to the outlet the plasma streamers would not reach the substrate, both in the simulation and experimentally.

To follow the spatial plasma propagation, for each of the two cases, the time evolution of the LF voltage, surface charge, and Ar^+ ion flux integrated over the entire glass substrate surface are shown. For six time instants, a color plot of the plasma density and electric field is provided, along with the electric potential distribution on the surrounding structures.

3.1. LF-only discharge evolution

The discharge evolution with LF-only on can be summarized in the following snapshots, which correspond to the six critical events identified in figure 2.

(1) 5.8 μs The cycle starts by applying a negative bias to the upstream electrode; the voltage is shown in black in the lower frame of the figure. At this stage, a positive streamer develops from the ground electrode to the upstream electrode. The streamer propagates on the surface of the alumina tube and covers the LF electrode in a few tens of nanoseconds. Consequently, a current peak 100 ns long with a maximum intensity of about 120 mA is recorded at the LF electrode. At the same time, the plasma expands in the direction of the glass substrate with densities of the order of $10^{15}\,m^{-3}$. Consequently, the substrate starts to charge negatively, and a sheath is formed up to reaching an equilibrium between the ion and electron flux. This initial stage of the substrate charging process is evidenced by a noticeable surge in argon-ion flux reaching the substrate, as depicted in the bottom graph of the figure.

(2) 18 μs The negative bias on the LF electrode begins to reduce; however, the glass surface remains negatively charged. The plasma retracts from the LF cathode because the dielectric surface facing the electrode is positively charged.

(3) 30 μs The voltage of the LF electrode is close to the ground potential; therefore the electric field generated is negligible. However, because of charges on the dielectrics, the positive streamer now propagates to the grounded electrode and is branched, because of electric field gradients. The surface of the glass maintains a nearly constant negative charge.

(4) 38.5 μs The LF electrode reaches almost its maximum positive potential. The LF electric field generated slowly drifts the ions to the tube outlet until their density is high enough to initiate a positive streamer to the substrate. The streamer covers the distance between the outlet and the glass surface in approximately 100 ns, and the formed channel is about a hundred micrometers wide. The streamer then propagates on the glass surface for about 1 μs. At 40.5 μs the entire glass is plasma covered as can be observed by the accumulated surface charge, which reaches a maximum charge of 30 nC (figure 2, *blue curve*). Consequently, a positive flux of ions can be detected on the order of $10^{16}\,s^{-1}$ (figure 2, *green curve*).

(5) 50 μs After the plasma covers the entire substrate, the glass surface is still positively charged; however, the charge is roughly constant and the electric field in the whole plasma volume is strongly reduced.

(6) 62 μs The low frequency electrode starts a new cycle with negative bias and again a positive streamer develops to the LF cathode. In the direction of the substrate, the electron flux restores negative charge on the glass surface.

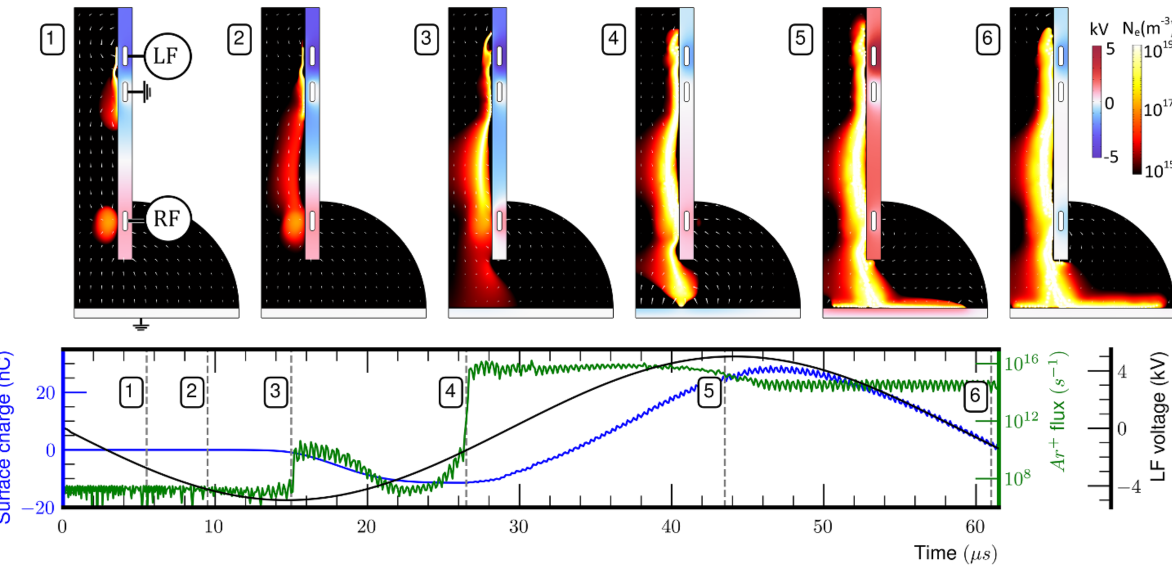

Figure 3. Results of the simulation of the discharge in the dual frequency RF+LF in argon. The RF discharge has already ignited at time $0\,\mu$s. (*bottom*) In the graph are reported as a function of time the integrated surface charge and Ar^+ flux on the whole glass substrate together with the LF electrode voltage. (*top*) Six critical events are identified, and the respective simulation snapshots of the electron density and electric fields vectors together with voltages in the dielectrics are illustrated.

The evolution of streamer discharge observed in the LF-only simulation is consistent with the literature. Operating a jet on a dielectric surface often results in the propagation of only positive streamers because they require lower voltages to initiate. The ion density in the streamer core was of the order of $10^{19}\,m^{-3}$ and was related to both Ar^+ and Ar_2^+.

The Ar^+ ionization requires a higher electron energy and therefore could only be observed on the head of the propagating streamers where space-charge separation induced high electric fields. At the same time, the decay of argon ions is relatively fast. Therefore, the Ar ionization process at the jet outlet was present only during streamer propagation to the glass substrate at stage (4). The impact of streamers on substrates has often been shown to cause damage to temperature-sensitive substrates as a result of localized energy loss.

The Ar_2^+ ions showed a longer lifetime and were preponderant in all other areas and when the streamer propagation stopped. Their generation, indeed, is mainly related to metastable state collisions (reactions 3,4 table 1) and to low-energy electron impact ionization reactions (reactions 7,8 table 1). However, their contribution should not be underestimated, as the charge pathway connecting the substrates with the electrodes exhibited high electrical conductivity ($Ar_2^+ \sim 5 \cdot 10^{17}\,m^{-3}$) and significant concentrations of metastable species ($Ar^* \sim 10^{16}\,m^{-3}$), leading to a memory effect for subsequent cycles.

3.2. RF+LF discharge evolution

The same computational model was then used to simulate the coupled configuration, where both the LF and RF electrodes were switched on. Similarly to the LF-only case, the evolution of the discharge is described through the time evolution of the integrated surface charge and Ar^+ flux on the whole glass substrate together with the LF electrode voltage, and six critical events are identified and presented in six different snapshots, as shown in figure 3.

(1) 5.8 μs The cycle starts by applying a negative bias to the upstream LF electrode. As in the previous case (when only the LF electrode was modeled), a positive streamer develops in the LF electrode region and covers the surface of the alumina tube in front of the electrode in a few tens of nanoseconds. The same peak currents of 100 ns and about 120 mA can be detected as in the LF-only discharge. However, here the LF electrode is further away from the substrate, and therefore, the plasma does not extend out of the jet and no charging is induced on the substrate. The ion flux on the glass is constant (approximately $10^7\,s^{-1}$) and is caused by the interaction with the RF plasma. At this stage the two discharges appear to be fully spatially and electrically separated.
(2) 9.2 μs In the LF region the plasma reaches density of up to $10^{19}\,m^{-3}$. The plasma shields the LF bias, however the region presents a negative potential. Conversely, in the RF plasma region, the voltage oscillates, exhibiting both concordant and discordant voltages within each RF cycle. As a results, a diffused plasma channel starts to connect the two excitation zones.
(3) 15 μs The plasma density in the channel connecting the electrodes reaches values of the order of $10^{18}\,m^{-3}$. The plasma expands in the direction of the substrate and thanks to the RF excitation the density starts to increase also close to the glass surface which charges negatively. This effect is also reflected in the ion flux on the substrate (figure 3, *green curve*), which shows an RF modulation.

(4) 26.3 μs In the region of the RF electrode the plasma eventually reaches densities of the order of $10^{19}\,\mathrm{m}^{-3}$. The plasma density obtained is distinct from other RF devices, emphasizing the activation of a specific ionization regime. Similar values have sometimes been reported in the literature in kHz [50] and RF [51] DBD jets. To support the validity of the result, the H_β line was recorded and the electron density was estimated by Stark broadening [52]. The results showed a plasma density at the jet outlet of the order of $10^{20}\,\mathrm{m}^{-3}$ (figure S4), which, even though at the limit of reliability of the method used, confirmed a rather high density of the plasma at the jet outlet.

The plasma density increases also close to the glass surface. As it reaches values of the order of $10^{18}\,\mathrm{m}^{-3}$ like a slow streamer propagates attracted by the negatively charged substrate. This propagation lasts several RF cycles. It seems that the ions accelerates to the substrate due to an electric field enhancement. Consequently, the Ar^+ flux increases by more than 5 orders of magnitude, and later on the plasma starts to propagate along the glass. The plasma requires more than 10 μs to cover the entire substrate and throughout this period the ion flux remains at the same order of magnitude. The maximum value of the Ar^+ flux is relatively similar to that of the LF-only discharge, while the plasma channel connecting the substrate with the electrodes is wider, reaching more than 400 μm.

(5) 42.5 μs The plasma covers the whole glass surface. The total surface charge is of the order of 30 nC, as in the LF-only model. Consequently, the electric field in the whole plasma volume is strongly reduced. However, contrary to the LF-only discharge, the Ar^+ flux remains of the order of $10^{15}\,\mathrm{s}^{-1}$.

(6) 62 μs A new cycle starts, the LF electrode is negatively biased again and the glass surface consequently becomes negatively charged. However, the ion flux to the glass remains constant, retaining the RF modulation.

The direct comparison of the two simulations highlights the differences in the discharge propagation and in the plasma interaction with the substrate. Even if the LF and the RF supplies are spatially separated, they are connected by the plasma itself. The resulting plasma is driven mainly by RF excitation, which changes both temporally and spatially the plasma volume expansion, hindering the streamer propagation. The LF may influence the drift of the ions. As a major consequence of the substrate treatment point of view, the flux of argon ions remains higher than $10^{15}\,\mathrm{s}^{-1}$ throughout the LF period. If the simulation continues into a subsequent cycle, the presence of background Ar_2^+ ions and argon metastables, which have longer lifetime, supports the maintenance of the plasma channel, resulting in a memory effect. Furthermore, the Ω regime also ensures continuous ionization in the bulk. As the voltage of the LF electrode transitions from negative to positive again, the sheath in front of the glass surface expands, leading to a new enhancement in the ion flux to the substrate and in the overall plasma density. Nevertheless, the plasma does not re-propagate along the glass surface because the area is already ionized. However, as the simulation progresses, the gas heating cannot be neglected further. Therefore, we stopped at the first cycle, which already suggests a propagation mechanism that can be compared to the experimental results.

3.3. The experimental comparison

To support the prediction of the simulation, ICCD images of the jet are shown in figure 4 for both the LF-only and RF + LF configurations. The time exposure is 500 ns; therefore, it can be considered a static condition for fluid dynamics. However, in both configurations, the filaments are not stable, but they move in space below the jet, and the time for the ignition of the streamer can shift by approximately ± 5 μs (figure 7 and S8) relative to the LF voltage from cycle to cycle. This instability is mainly due to variations in the surface charge on the dielectrics. The images presented were obtained by synchronizing the exposure with the LF voltage and varying a time delay, however, since they correspond to different LF cycles and the plasma is not stable, their association with the surface charge and LF signal presented in figure 4 was reconstructed. Therefore, the positioning of the time in figure 4 should be considered non-quantitative and only indicative of the time stage relative to the LF cycle for comparison with the simulation.

As can be observed in both configurations, the streamers propagate vertically out of the jet, supporting the laminar flow condition [29]. With LF-only, the streamer propagates nearly straight, perpendicular to the substrate, and then propagates on the glass surface. Light emission is concentrated in the filament core, which is no more than 100 μm in diameter. Light emission is concentrated in time stage (4) where a positive surface charging step is detected on the substrate. This step always occurs during the positive slope and positive values of the LF voltage, in agreement with the simulation results obtained. In addition, the time duration of the charging in the simulation and in the measurement is fully comparable and on the order of 500 ns. Outside of time stage (4), light emission is off, as are the ionization and the Ar^+ flux to the substrate in the simulation.

In the dual frequency configuration, the luminous filaments are more diffused, and as they reach the substrate, they show a bending before propagating on the glass surface. The absence of a perpendicular impingement of the plasma channel on the substrate underscores the different propagation mechanisms and is consistent with the simulation results. In the simulation, the plasma channel is also broader, and light emission remains continuous throughout the entire LF cycle. The emission is mainly visible in the plasma column connecting the jet to the sample. Only in stage (4) an additional light emission appears to start from the substrate and then propagates on the glass surface and through the whole column. This increase in light emission corresponds to the positive charge step of the sample, which, this time, lasts about 2 μs. The general description of the propagation mechanism obtained by light emission imaging suggests that the results obtained in the model, even with the approximation of neglecting gas heating and air interaction, are qualitatively reliable.

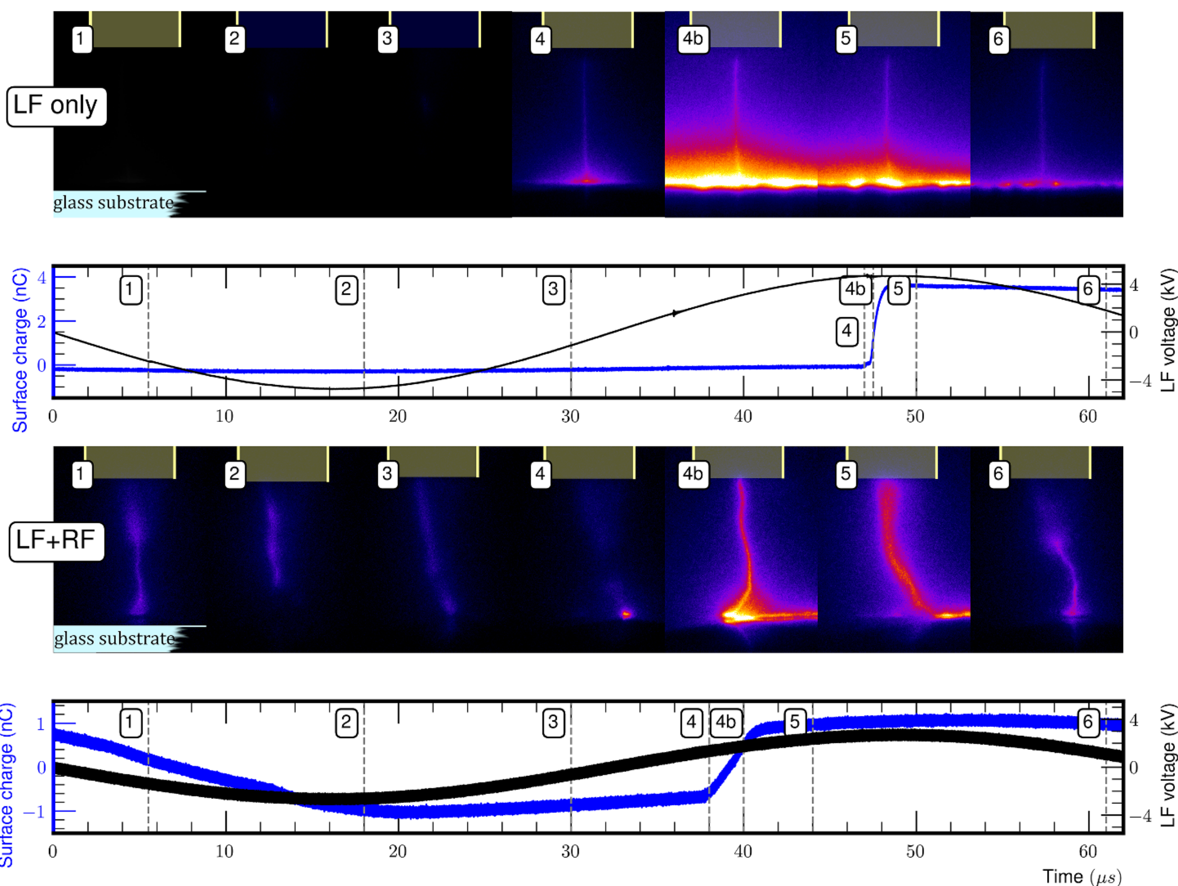

Figure 4. ICCD images of the plasma jet on a glass substrate (500 ns exposure) in the two configurations: (*left*) (a) LF-only and (*right*) (b) RF+LF. The capture was synchronized with LF voltage and the surface charge recorded during a single cycle is also reported. The ICCD images were not acquired across different cycles relative to the electric signal; they are instead associated with the time stages discussed in the simulation ((1)–(6)). From cycle to cycle streamer or γ-regime ignition can shift by several microseconds (figures 7 and S8) and the filaments spatially move. As a visual aid, the sketch of the jet outlet featuring the alumina tube, the coaxial external LF or RF electrodes and the glass sample are superimposed onto the photos.

To further validate the accuracy of the RF+LF simulation predictions, we recorded the electrical signal and optical emission as a function of time with the jet device in the same configuration as in the model. The only relevant difference was that the device was operated in an open air rather than in a full-argon environment. LF and RF voltages were continuously monitored and the RF power was kept constant at 15 *W*. We also recorded the charge on the substrate and the light emitted close to the glass substrate. When the LF voltage was set to 1 kV, the substrate showed a capacitive coupling with both RF and LF. However, very few photons could be detected (figure S8). This suggests that at such low LF voltage the ion drift to the substrate was probably insufficient to initiate plasma propagation outside the jet.

As the LF voltage increased, the plasma visually propagated outside the jet and on the glass surface. Figure 5 compares the experimentally recorded charge on the glass surface and the related optical emission to the surface potential from the simulation at position $1a$ (figure 1) on the glass. The optical emission data was obtained with 150 accumulations.

As a first observation, it is evident that the optical emission persists throughout the LF cycle, indicating the continuous presence of an ionization process. This finding is fully in agreement with the simulation results, which attribute the primary ionization role in the dual-frequency discharge to the RF excitation.

In addition, just below the alumina tube on the glass surface the simulation shows a fast increase, like a step, in the surface voltage. This event corresponds to stage (4) in the description previously presented and is associated with the RF plasma being accelerated to the glass surface, which is negatively charged. At this time, the LF voltage is small; therefore, the external LF field is negligible. Therefore, the sources of the electric field are the RF electrode and the negative charge on the glass. With respect to the relative oscillations amplitude, the experimental step height matches well with the simulation. Although the surface voltage on the glass cannot be measured directly through experiments, it is proportional to the charge that is collected. Therefore, the measured step supports the simulation predictions.

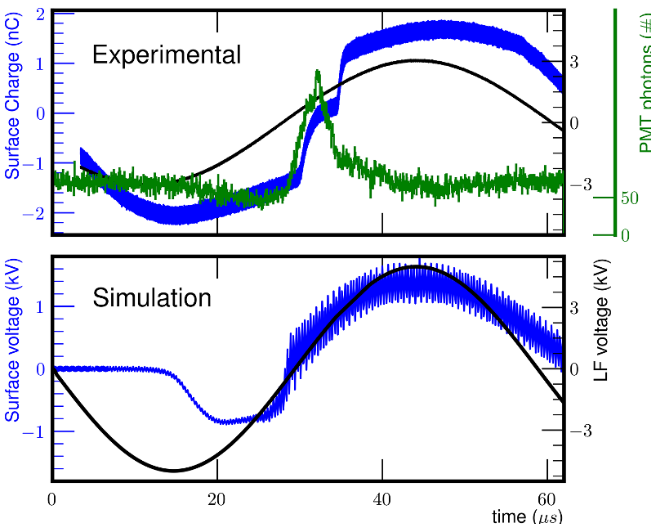

Figure 5. Comparison of simulation results (bottom) with experimental data (top) across an LF cycle. The simulation shows the LF voltage and the glass surface voltage at position $1a$ in figure 1, while the experimental data present the LF voltage, the surface charge on the glass, and the optical emission near the substrate, represented by the histogram of the photons detected by the PMT. The optical emission is obtained with the accumulation of 150 cycles.

Moreover, the step duration exceeds $1\,\mu$s in both the experimental and simulated results, compared to the approximately 100 ns typical of streamer discharges. This duration corresponds to more than ten RF cycles. The occurrence of multiple steps in the experimental data is likely attributed to the existence of various filaments within the discharge.

The experimental data, therefore, validate the overall description of the dual frequency discharge where the RF hinders the propagation of the positive streamers by providing a pre-ionized media. Moreover, LF induces an ion drift enhancing ionization close to the substrate during a specific time frame within the LF cycle.

4. Discussion

4.1. Plasma regime on the glass surface

The data collected from this experimental jet setup exhibited a notable resemblance to the dual-frequency excited parallel plate configuration discussed in literature [17]. Indeed, in both configurations, the plasma is driven by RF excitation, while LF predominantly affects the ion drift. Thus, the jet would likely exhibit the coexistence of the Ω and γ regimes, similar to parallel plates. Furthermore, this coexistence can may be observed on the substrate at a distance of centimeters from the electrodes. To confirm that this is the case in our jet configuration, we considered the simulation during an RF cycle at three different stages: when the plasma reached the substrate (4), during the positive (5) and negative (6) phases of the LF voltage (figure 6). The corresponding 2D plasma densities taken from figure 3 are reported on the left to facilitate visualization of the respective condition. In the same plasma density map, the red lines indicate the positions where the various parameters are measured relative to the distance from the glass surface. Different regions of the discharge can be easily identified: near the glass, the sheath is visible, whose thickness oscillates as a function of RF. Above the sheath, there is a high plasma density layer that confines the positive net charge zone (indicated by the black contour). Proceeding further from the glass substrate, at stage (4) the bulk of the plasma column is found. In stages (5) and (6) there is a zone without plasma since it is propagating horizontally on the glass surface. The complete representation of the space charge density together with the deposited power on electrons is shown in the 2D maps in figure 6, right column.

Stage (4) is shown in the first row of figure 6. At this time, the plasma has not made contact with the surface so far. In the 2D plasma density map (right) the glass appears in blue, indicating a negative potential relative to the ground. Thus, the total charge on the glass is negative. In the graph in the second column, indeed, the electric potential of the glass in position $1a$ (green dashed line) settles at values that remain negative throughout the entire RF cycle. The surface potential oscillates as a function of the RF and exhibits a very small phase delay with respect to the RF electrode voltage (blue dashed line). The sheath voltage, calculated as the potential difference between the glass surface and the region beyond the positive net charge boundary, is represented by a dashed red line on the graph. The sheath potential follows the temporal evolution of the voltage difference between the RF electrode and the glass surface.

At the peak positive voltage of the RF electrode, the sheath exhibits a voltage drop of around 1 kV. The sheath thickness is approximately 0.5 mm in stage (4). By examining the Ar^+ production rate and the electric field E_z perpendicular to the glass surface in the maps, one can see that this voltage maximum in the sheath aligns with an increase in the field toward the substrate and a noticeable increase in ionization. This ionization is promoted by secondary electrons accelerated through the sheath, which correspond to the γ excitation regime. This excitation appears to be active only during a small fraction of the RF cycle and is probably related to the sheath voltage values [11]. The acceleration of the ions to the glass surface observed in the stage (4) of the simulation is reality fostered by the activation of this additional ionization mechanism.

On the opposite boundary of the positive net space charge region, above about 1 mm from the glass surface, along the plasma column that connects the substrate with the electrodes, the Ar^+ production rate is also modulated by RF. However, it does not appear to be affected by the plasma interaction with the glass, showing a frequency twice that of RF. In addition, in terms of phase, the maximum ionization rate occurs when the RF voltage crosses 0 V, when the alternating displacement current between the sheath and the RF electrode reaches its maximum. This mechanism is also confirmed by the electric field E_z, which alternates through the RF cycle corresponding to the currents moving back and forth. Therefore, in the plasma column, the excitation mechanism can be associated with the Ω mode. The Ω-mode and the γ-mode seem therefore to coexist in different regions of the discharge, even on the substrate.

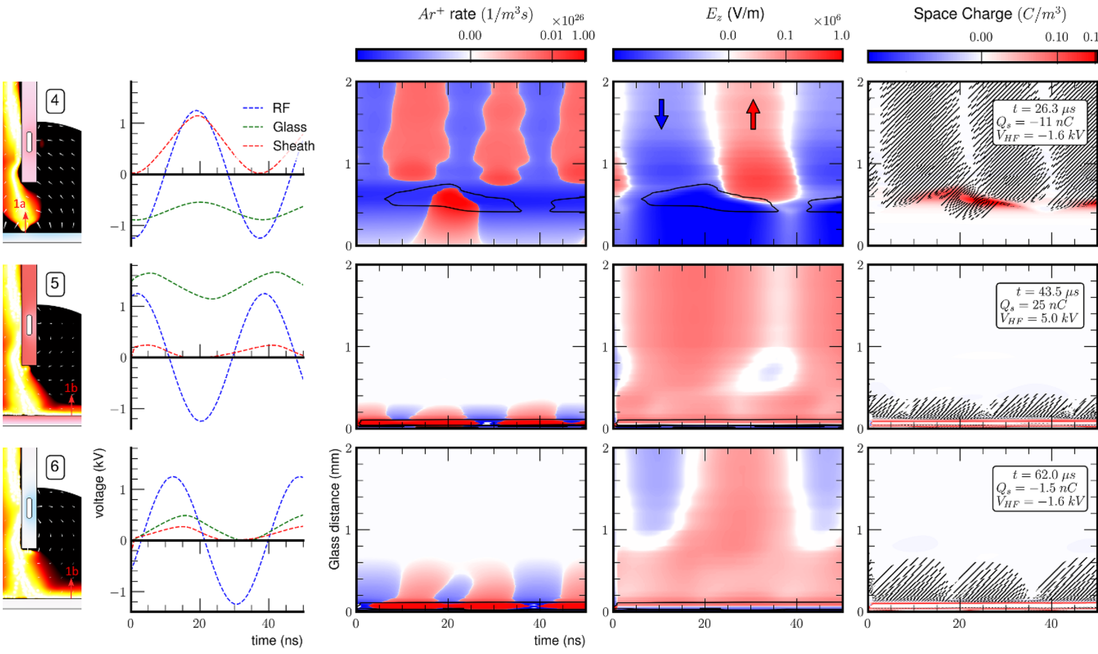

Figure 6. Simulation results during an RF cycle for three of the critical events identified in figure 3 ((4) 26.3 μs (*top*), (5) 42.5 μs (*center*) and (6) 62.0 μs (*bottom*)) for the dual-frequency RF+LF configuration. On the left are reported the relative 2D maps of the plasma density of figure 3 indicating location 1*a* and 1*b* in red from which the data are extracted as a function of the distance from the glass surface. The data are then presented as a function of time. The first column includes line graphs of the voltage of the RF electrode, the glass surface, and sheath drop. The 2D maps show as a function of the distance form the glass surface the rates Ar^+, the component of the electric field E_z orthogonal to glass surface, and in the last column, the space charge and the deposited power on electrons (black pattern). In the 2D maps, the black lines correspond to the contour region of positive charge, which identifies the sheaths.

The same representation of discharge evolution is offered by the power dissipation P in the plasma, evaluated as the scalar product between electron flux and force on electrons $P = e\vec{\phi}_e \cdot \vec{E}$. In the 2D maps, the region of power dissipation is shaded by a black line pattern. In the plasma bulk, the power dissipation is modulated with a frequency twice that of the RF. Within the sheath, maximal power dissipation occurs at the peak voltage of the sheath, coinciding with the highest electron flux and electric fields and therefore with the same frequency of the RF.

On the other hand, the Ar_2^+ production rate at this stage does not show any modulation during the RF cycle. Indeed, as we already reported looking at the evolution of discharge on the LF cycle scale, Ar_2^+ is mainly produced by reactions that involve metastable states.

In stages (5) and (6) the plasma has already spread onto the substrate as a surface discharge. For these stages, the radial position 1*b* was chosen far from the jet axis to examine whether the propagation regimes were consistent throughout the glass surface.

In stage (5), the LF voltage is close to its positive maximum and the glass surface appeared to also be positively charged, showing an average voltage higher than the RF amplitude. The resulting voltage across the sheath is less than 100 V. Therefore, even if the ion flux on the glass enables secondary electron emission from the surface, their acceleration is limited. As a consequence, γ excitation cannot be initiated. The sheath on the substrate can be identified by the region of the electric field E_z pointing to the substrate (in blue), which is approximately 0.05 mm thick in stage (5). Beyond the sheath lies a 0.3 mm thick layer characterized by a high plasma density. This layer can be easily identified in the power dissipation pattern and in the Ar^+ production rate map, since both depend on the presence of electrons. Both parameters exhibit modulation at twice the RF frequency. Ionization in this region, indeed, is driven by propagation of the RF electric field along the plasma channel, parallel to the glass surface. Therefore, ionization occurs in the Ω regime in this layer as well as in the plasma column and is continuous even during the positive part of the LF cycle. This observation agrees with the continuous ion flux observed on the glass surface presented in figure 3 and is also corroborated by experimental optical emission results. In the direction orthogonal to the substrate, the E_z field confines the electrons in the plasma channel, pushing them back on both sides.

At stage (6), the LF voltage enters in its negative part of the cycle; however, the glass still shows a positive voltage on the surface. Therefore, the sheath voltage is on the order of a few hundred volts. The ionization process and the structure of the layers are very similar to those observed at stage (5). However, the positive charge on the glass is reduced; therefore, the plasma layer will expand later on, reaching again a thickness of about 0.5 mm, as in stage (4).

As a result, we can conclude that the simulation suggests the presence of the Ω regime near the substrate, which is always active throughout the whole LF cycle. The excitation is enabled by the RF electric field propagating vertically to the substrate in the plasma channel below the jet to

the substrate and then radially parallel to the surface of the glass. The voltage on the glass surface is determined by the LF voltage, which strongly affects the sheath thickness. As the voltage drop in the sheath is above a certain threshold, the γ regime is activated as additional ionization mechanism. However, the γ mode is switched on only under favorable conditions of both RF and LF voltages. Thus, the discharge near the substrate operates in both RF regimes.

4.2. Observation of the Ω and γ coexistence

The optical emission from de-excitation processes or quenching and recombination in a plasma can also be an indication of the presence of ongoing ionization. By selecting a specific wavelength, it is possible to improve this connection, such as, for example, using the Ar ($3p^54p \rightarrow 3p^54s$) lines [43]. If there is no self-absorption, their intensities are representative of the excitation rate of their upper states [16]. In our case, we decided to observe the entire emission spectrum close to the substrate without any spectral filtering. Nonetheless, since we operate in pure argon, the most intense emission lines within the spectrum correspond to argon in the 700–900 nm range, which primarily pertain to the $3p^54p \rightarrow 3p^54s$ transitions. This configuration enhanced the optical signal while maintaining a nanosecond-scale temporal resolution, required to scan an RF period of approximately 37 ns.

The optical signal was collected on a PMT as a function of time in the LF cycle after synchronization with the RF signal (figure 7). Light was collected from a 200 μm slit, with a length of 1 cm, positioned parallel to the glass surface at a distance of 0.5 mm. The analog signal of the PMT was then processed to obtain the histograms of the number of photons detected by the PMT, using 200 acquisitions. Electrical signals such as the voltage of the LF electrode and the charge collected in the sample for the whole 200 acquisitions are shown in figure 7 to correlate the emission with the different stages of plasma propagation during the LF cycle.

As shown in figure 5, at the moment when the LF voltage crosses zero with a positive slope (time stage (4)), there is a noticeable step in the collected charge, accompanied by an increase in optical emission. The reproducibility within the different cycles is somewhat limited on the microsecond scale, and the maximum charge collected on the glass may vary, but the overall behavior is preserved. The optical emission is continuous through the whole LF cycle as already observed in figure 5. The RF modulation cannot be visually resolved in the graphs on the LF timescale, therefore, on the right column is presented the histogram of the optical emission for a series of four RF periods. As a reference of the RF cycle the modulation of the surface charge on the glass, normalized in arbitrary units, overlaps with the optical signal.

The zoom on the RF scale is proposed for four selected time periods that span the LF cycle, corresponding to different time stages of the simulation. At 20 μs the LF voltage is positive and the glass is also positively charged. In this case, the conditions

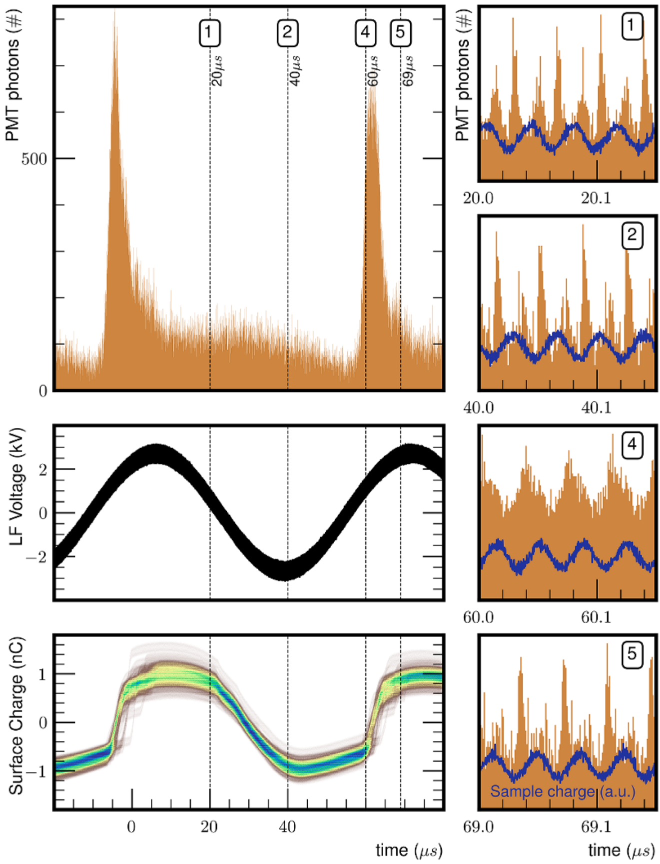

Figure 7. (*left*) The left column shows the correlation among the optical emission with the electrical signals such as the LF electrode voltage and the charge collected on the glass surface. The results are obtained through 200 accumulations with maximum LF voltage of 3 kV and 20 W of RF power. (*right*) The right column shows the correlation of the optical emission with the RF modulation of the charge on the glass surface (a.u.). Four specific times, 20, 40, 60, and 69 μs, corresponding to different time stages of the simulation ((1), (2), (4), (5)) have been selected and indicated in the LF cycle for reference.

are similar to stage (1) of the simulation (figure 3). The sheath voltage is therefore low and only the Ω regime is expected. In figure 7, indeed, the emission is not constant but is modulated with a frequency that is twice the RF. In addition, this emission is out of phase of 90° with respect to the maxima or the minima of the charge on the sample. The frequency and phase characteristics confirm the presence of the Ω regime close to the substrate. The result, moreover, agrees well with the reduced thickness of the sheath.

As the LF cycle proceeds at 40 μs the LF voltage is negative (stage (2)), as is also the charge on the glass surface. At these time frames the condition is similar to the previous stage, and in discharge is present the only Ω regime. The optical emission, indeed, confirms the Ω ionization mechanism, keeping the modulation of twice the RF and the 90° phase shift with respect to voltage. However, from the general emission in the LF it can be observed a reduction of the overall number

of photons recorded. This may be linked to an expansion of the substrate sheath, which pushes back the ionization region far from the glass surface. The probed region of the optical emission is in fact 0.5 mm above the glass surface.

Time 60 μs is selected exactly at the step in surface charge, where an ion flux is therefore expected. This condition resembles the simulation stage (4) (figure 6), when the plasma accelerates to the substrate. At this time frame, the electric field in the sheath is of the order of 1 kV and the γ mode is activated. In the optical emission, indeed, we see the presence of an additional peak among the Ω ones, more intense, with the frequency of the RF and in phase with the maximum on the surface charge. These characteristics fully coincide with the γ excitation mode. Therefore, the experimental data validate the coexistence of the Ω and γ regimes close to the substrate and also agreed on their position relative to the glass surface and the timing with respect to the LF cycle.

After the positive step the charge collected on the substrate still shows a slow increase, which agrees with the simulation. However, the optical emission is strongly reduced and mainly presents ionization in the Ω-regime. As the surface is positively charged after the step, in fact, the substrate sheath is again reduced, even if the positive flux of Ar ions to the substrate is maintained because of the increasing voltage of the LF electrode. However, the optical emission is collected from an area located 0.5 mm above the glass, resulting in the emission of the γ regime being no longer observed.

4.3. Self-sustain in γ regime

The transition from Ω mode to γ mode can occur only if the ionization mechanism initiated by the secondary electrons emitted by the surface induces a self-sustaining process. This aspect was already explored by Robert *et al* [19] in a detailed modeling effort of dual frequency planar plate discharge in a Penning gas process. In particular, the model was refined with the addition of excimer emission ionization. In this work, we did not include radiation as an ionization source; nevertheless, we used the same analysis to further describe the interaction of the jet with the substrate and confirm the presence of the γ-mode. If the secondary electrons emitted by the wall can generate a self-sustaining discharge mechanism, this means that they produce more ions in the sheath for each electron [17, 53]. The self-sustaining criterion can then be summarized in

$$\frac{\gamma_i \Gamma_{i,\text{sheath}}}{\Gamma_{\text{SEE}}} > 1, \tag{7}$$

where γ_i is the secondary electron emission coefficient, $\Gamma_{i,\text{sheath}}$ is the number of Ar^+ ions produced per unit of time in the sheath, and Γ_{SEE} is the secondary electron emission flux from the wall [18]. $\Gamma_{i,\text{sheath}}$ was obtained by integrating the rate of ion production into the sheath thickness, which was identified by the region of negative field E_z close to the glass as a function of time. The criterion was calculated at the respective positions $1a$ and $1b$ in the glass for stages (4)–(6) of figure 3. The self-sustaining parameter is shown

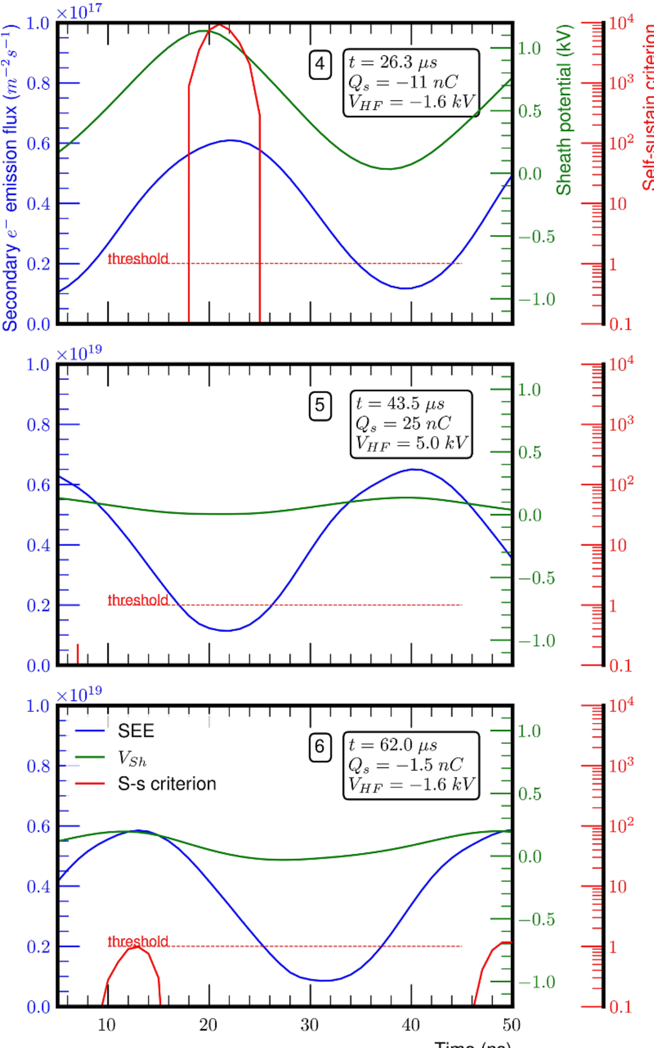

Figure 8. Evaluation of the self-sustain criterion starting by the simulation results resolved within an RF cycle for three different events identified in figure 3 ((4) 26.3 μs (*top*), (5) 42.5 μs (*center*) and (6) 62.0 μs (*bottom*)) for the dual frequency LF+RF configuration. Secondary electrons emission flux and sheath potential above the glass surface are presented in the left axis of the graphs.

in red in figure 8 together with the secondary electron emission flux and the sheath potential. In stage (4) the plasma is reaching the substrate, which is negatively charged. The sheath potential reaches more than 1 kV as its thickness is close to 0.5 mm. Secondary electron emission follows the ion flux and their energy the sheath potential. However, the criterion for self-sustaining is satisfied only during a small part of the cycle, when the emitted electrons gain enough energy to boost ionization.

Compared to stage (4), in (5) the secondary electron flux increased by two orders of magnitude. The improvement was strongly related to an increase in the plasma density as a consequence of the interaction with the substrate and the propagation on the dielectric surface. Despite the increase in emitted electrons, the γ-mode was not initiated. The surface of

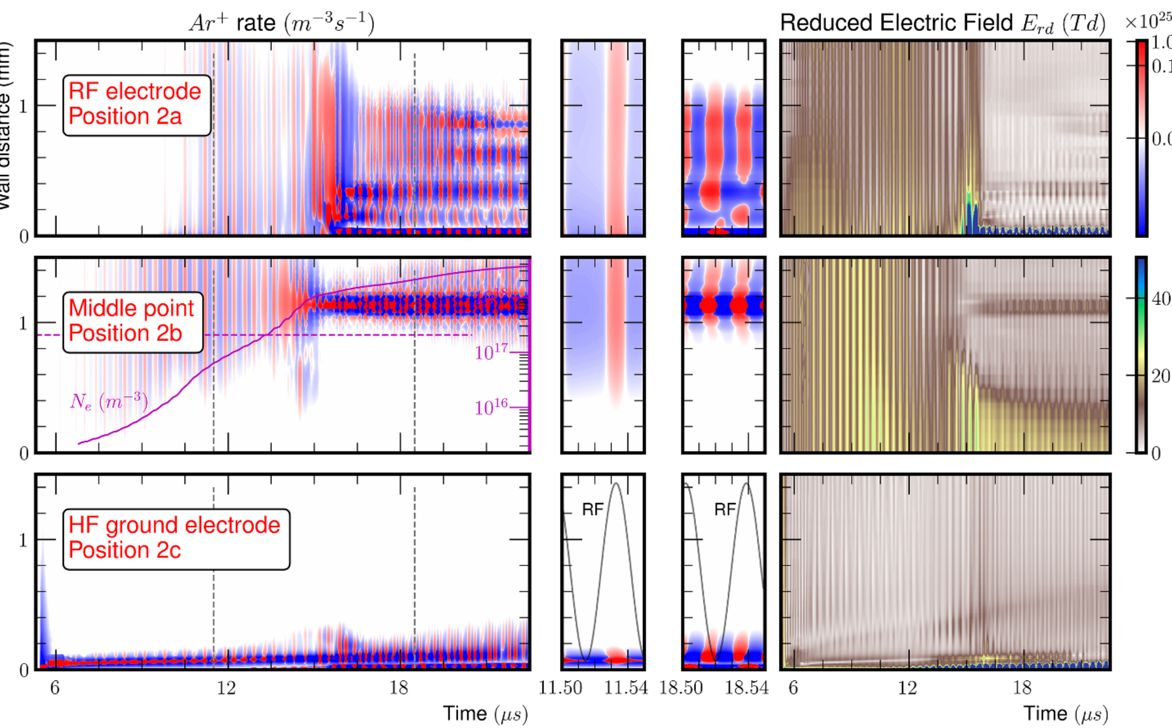

Figure 9. Results of the simulation during the connection between the LF and the RF discharges. The distance from the alumina wall is reported on the vertical axis. The *x*-axis shows the time for three different positions in the tube: (2*a*) at the border of the RF and (2*c*) LF ground electrodes and (2*b*) in the middle between the two. The 5−20 μs range graphs have a resolution of 0.1 μs, while those with a range of an RF cycle of 0.5 ns. The time corresponding to the RF cycles is indicated as dashed lines in the wider-range plot. In blue/red is presented the Ar^+ production rate, while in brown/blue the magnitude of the reduced electric field. In the middle graph of the left column is also reported the time evolution of the plasma density at a distance from the alumina wall of 0.9 mm.

the glass was indeed positively charged and the plasma sheath voltage oscillation was lower than 100 V. Under this condition, the electron did not gain enough energy to promote a self-sustaining ionization mechanism.

As the LF voltage decreased in stage (6), the electron flux remained of the same order of magnitude, since the plasma density was similar. However, the positive charge on the glass decreased and the sheath voltage began to rise again with an oscillation of about 200 V. This potential was enough to shift the self-sustaining parameter close to the threshold; as the LF voltage continued to decrease, the γ-mode was again ignited. Therefore, as expected, the criterion parameter is not related to the plasma density and to secondary electron emission itself, but rather to the energy gained by the electrons in the sheath.

The model considered three reactions that can lead to the production of Ar^+: electron impact ionization with argon in the ground and in the excited state (table 1 No. 5, 6), and associative ionization between two metastable argon species (No. 10). In the model, no Penning reactions were included because it considered only argon as a gas species. From the reaction rates obtained in the simulation, reaction No. 5 was the only one connected to ignition of the γ-mode. This can be explained by its direct relation to the number of electrons and by its dependence on the electron temperature. Reaction rate No. 6 is also derived by solving the Boltzmann equation; however, the density of the excited argon with respect to the base gas is one order of magnitude lower. Instead, the dependence of the associative reaction on time is limited because the metastable species do not interact with the electric field and the reaction does not involve the electrons. On the other hand, the role of the excited states becomes prominent in the Ω-mode region, where the electron temperature is lower.

In fact, the overall description coherently describes the substrate as an electrode participating in the discharge and all electrodes as somehow connected by the plasma. Therefore, the coexistence of different regimes observed in parallel plate devices [17] also adapt well to the dual frequency APPJ.

4.4. The RF and LF plasma merging

To highlight that it is the same plasma that connects all electrodes with the same hybrid regime, we present the discharge evolution between the RF and LF electrodes in figure 9. The interval of connection of the two separated discharges was observed as a function of time and distance from the alumina wall. As shown in figure 3, channel formation is a relatively slow process. It starts approximately 5 μs after the initiation of the LF voltage supply and ends around 20 μs, encompassing stages (1), (2), and (3). We selected three different positions, reported also in figure 1: (2*a*) at the RF electrode border, (2*c*) at the ground electrode, and (2*b*) in the middle between the two.

Before 6 μs, the two discharges are separated. Plasma densities are of the order of $10^{15}\,m^{-3}$ at the positions 2*a* and 2*b*

(figure 9 in the middle graph of the left column, right y-axis), and the ionization rate is negligible. In location $2c$, the plasma density is higher, as the positive streamer discharge extends also on the ground electrode. In this position $2c$, the ionization process has already started and is visible because of the higher plasma density (figure 9 left column). The reduced electric field at this stage (figure 9 right column) is lower than 10 Td. However, we can observe that the reduced electric field oscillates in the tens of nanoseconds scale; therefore, we can link its origin to the RF electrode.

As a result of this oscillating electric field, the electron density between the electrodes slowly increases. The ionization begins to rise at the middle point $2b$ at a distance of about 1 mm from the surface of the alumina wall. Close to the ground electrode, at position $2c$, ionization remains mainly constant, while close to the RF electrode, at $a2a$, the increase in ionization rate arrives approximately 5 μs later. As the plasma density grows, the reduced electric field also increases, reaching values of the order of 30 Td and maintaining its oscillating character. This increase in electric field is due to the LF voltage, which continues to decrease its negative value until its minimum at 14 μs. Later, as the plasma density reaches a density higher than $10^{17}\,m^{-3}$, the ionization loses its diffused character on the millimeter scale, and a more dense channel is formed connecting the electrodes. In the ionization region there is also a drop in the reduced electric field, which turns back on the order of 10 Td.

To better investigate these two regimes, the Ar^+ reaction rate is resolved within an RF period before and after the critical point at about 14 μs (middle columns in figure 9). After the transition at about 18.5 μs the ionization process concentrates in a channel of a few hundred micrometers at the middle point $2b$ and clearly shows a frequency double that of the RF. Therefore, the ionization process can be linked to the Ω-mode, the same which later occurs in the plasma column connecting the substrate. However, before the transition at about 11.5 μs, the Ar^+ reaction rate shows the same periodicity of the RF in all three positions considered $2a$, $2b$, and $2c$. The voltage in the LF region is, indeed, negative, therefore, during the positive half-cycle of the RF electrode, the reduced electric field can reach values of 30 Td. The diffused character of the ionization process, which shows a maximum at the middle point $2b$ and the slow growth of the density, which lasts tens of microseconds, suggests that this electric field is sufficient to enable like a pulsed diffused avalanche discharge. This ionization mechanism, therefore, shows the periodicity of the RF as can be observed from the zoom at 11.5 μs in figure 9. As the plasma density reached $10^{17}m^{-3}$, the electric field is confined in the sheaths in front of the electrodes and the transition occurred.

After the transition, as the plasma density increases close to the electrodes in positions $2a$ and $2c$, the electric field also increases in the sheaths, reaching values of up to 50 Td with RF modulation. In the sheath, the γ regime can be initiated correspondingly, as can be observed by modulation at the RF frequency in the figure close to the alumina wall at the height of the electrodes. Therefore, once the channel connecting the electrodes is formed also inside the tube, we can observe the coexistence of the two different regimes also in the channel connecting the electrodes.

4.5. The plasma/substrate interaction control

Therefore, in the discharge processes presented, different modes with their own periodicity overlap: an Ω-mode with a frequency twice that of the RF and a γ-mode with the same frequency as the RF and a LF capacitive coupling; moreover, the γ-mode switches on and off with the frequency of the LF. These dynamics in non-linear media like the plasma generate the propagation of the respective harmonics. These harmonics were easily detected on the substrate charge signal in the frequency domain, which could be acquired separately from the time domain in our oscilloscope. In particular, in addition to the harmonics of the RF and LF frequencies, at each RF harmonic, the pattern of the LF harmonics overlapped (figure S3), again highlighting the interconnection of the frequencies in the ionization process.

The described dual-frequency APPJ showed the ability not only to obtain a plasma plume in the open air as the RF jets but also to excite the plume in RF regimes on the substrate surface, enabling a uniform flow of ions to the treated substrate. A clear advantage would be the possibility to control such a plasma/surface interaction. To show that, we measured the charge on the glass surface as a function of the LF voltage for different values of the distance from the jet and the maximum LF voltage (figure 10). A distance variation in the range of 5 mm did not appear to introduce any changes in discharge characteristics. The maximum charge on the glass changes coherently as a function of the capacitance, as can be observed by the progressive reduction of the slope of the straight part of the loop as the distance increases. However, the steps in the positive part of the LF cycle are always of comparable size and duration, highlighting the mitigation effect in streamer propagation linked to the RF bias. In addition, the plasma power delivered to the sample, calculated as the area included in the loop, remained constant throughout the range of distances considered. Therefore, the distance between the sample and the jet showed a limited impact on the interaction, which facilitated the application of the dual frequency jet for surface treatments. This behavior is also in agreement with the thermal load measurements (figure S5), which showed no changes as a function of the copper plate distance.

On the other hand, the change in the maximum LF voltage allowed us to tailor the interaction of the plasma with the sample glass surface. At 1 kV the coupling is only capacitive, and no power is delivered to the plasma on the surface. Visually, the plasma did not even propagate on the glass surface. As the voltage increased at 2 kV, the plasma spreads over the dielectrics, and the first charge steps described above began to appear. Their duration is always on the microsecond scale, and the charge per streamer collected on the surface is limited. The Q-V curve now exhibits a loop, which proves the energy dissipation in the plasma at the surface of the substrate. As the LF voltage increased further, additional charging steps were added during the positive part of the LF cycle, respectively, improving the power delivered. The increase in steps

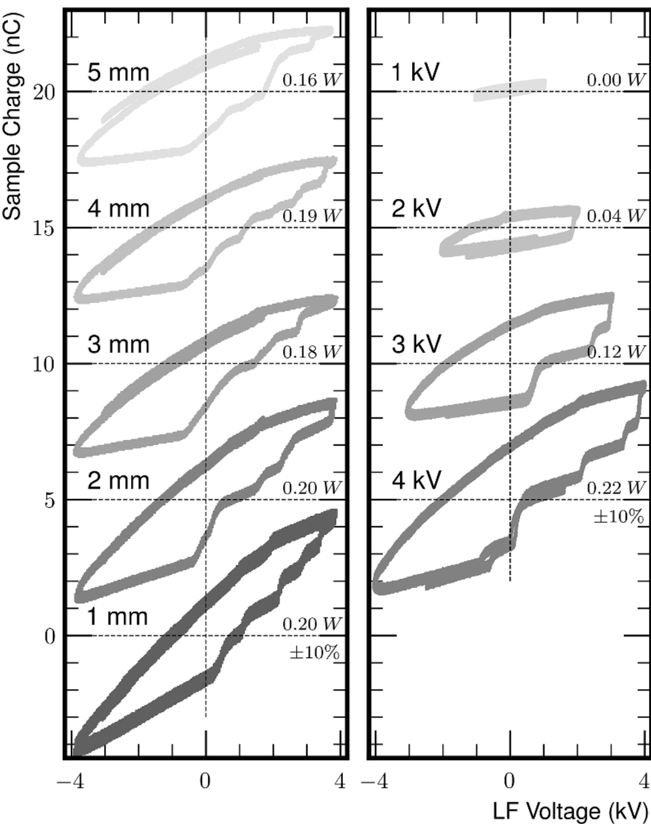

Figure 10. Charge on the glass sample as a function of the LF electrode voltage at different distances of the tube outlet from the substrate (left) and of the LF maximum voltage (right). The total power calculated as the area included in the loop is reported with an error of ±10%.

is probably due to the increase in the number of filaments reaching the substrate. The LF maximum voltage was therefore able to control the power delivered to the plasma close to the substrate, confirming also in an APPJ the possibility to tame the plasma surface interaction by means of the dual frequency configuration.

5. Conclusions

Based on both simulation and experimental results, it can be concluded that the coaxial APPJ exhibits excitation coupling in dual frequency mode, similar to what occurs in parallel plate setups. This coupling occurs even when the electrodes are spaced a few centimeters apart and can also be detected on the insulating substrate exposed to the jet.

Plasma evolution in the jet was first described by modeling the discharge in a 2D revolution geometry for approximately 3 cm. The model was validated by verifying the continuous ionization through the LF cycle. Furthermore, the model and the optical emission measurements agreed in showing the coexistence of the Ω and γ regimes in the discharge. The Ω mode provides continuous ionization in the bulk of the plasma, whereas the γ mode occurs in the sheaths only when the voltage drop is sufficient to initiate a self-sustained discharge.

The advantages of such a discharge configuration can therefore be summarized in enhanced ionization and high plasma density on the substrates, absence of streamer propagation, and therefore no localized heating. At the same time, a continuous flux of ions is ensured to the substrate. In addition, it was shown that the interaction with the substrate is not sensitive to the jet distance and that the substrate coupling can be controlled by the LF voltage.

As a drawback, the dual frequency discharges maintain an RF character which is characterized by low electron energy and potential gas heating. In addition, the coupling of the substrate leads to the flow of tens of milliamperes current to the treated objects.

The dual frequency APPJ, therefore,emerges as an interesting configuration for processes implementation. A notable application is the deposition of coatings on sensitive substrates, where achieving uniformity and conformability is crucial [24, 25, 54]. The advantage is not only that streamer propagation is hindered; therefore, localized damage, heating, or defects in the coatings are avoided, but also that low-power RF discharges do not switch off even in the presence of precursors in the plasma [55].

Another field of application is related to processes that require large fluxes of electrons and ions to the substrate. The dual frequency can, indeed, be efficient in reduction processes as, for example, in the deposition of metals for surface wiring or in enabling field-assisted ion exchange processes. Additionally, the dual-frequency APPJ holds potential for advancing plasma-liquid interface studies. In the region between plasma and liquid and, in particular, in the sheath, there is a peculiar environment that still has to be fully understood [56]. The dual frequency with the high flux of ions and electrons and with the potential control of the γ regime would, indeed, widen the available process variables.

The examples provided pertain to the field of materials science; nonetheless, the features of the dual-frequency APPJ can also facilitate progress in environmental applications and plasma medicine. In the latter scenario, managing the ion flux with LF and being unaffected by substrate distance can aid, for instance, in regulating the plasma dose administered to patients.

Data availability statement

All data supporting the findings of this study are included in the article (and any supplementary files).

Acknowledgments

This work has been supported by the Project 'VOGA'N WATER—Vertically Oriented Graphene-Assembled Nanostructures for WATER purification' funded by the MUR Progetti di Ricerca di Rilevante Interesse Nazionale (PRIN) Call 2022—Grant 20223CWFZT and by the Project iNEST funded by the program Next Generation EU of the European Union (PNRR—Missione 4-2-1.5). CloudVeneto is acknowledged for the use of computing and storage facilities.

Conflict of interest

The authors declare that they have no known competing financial interests or personal relationships that could have appeared to influence the work reported in this paper.

ORCID iDs

Alessandro Patelli https://orcid.org/0000-0001-7662-4352
Silvia Giuditta Scaltriti https://orcid.org/0009-0004-5960-7779
Arturo Popoli https://orcid.org/0000-0002-0990-8053
Emilio Martines https://orcid.org/0000-0002-4181-2959

References

[1] Massines F, Sarra-Bournet C, Fanelli F, Naudé N and Gherardi N 2012 *Plasma Process. Polym.* **9** 1041–73
[2] Weltmann K D and Von Woedtke T 2011 *Eur. Phys. J. Appl. Phys.* **55** 13807
[3] Bruggeman P J, Iza F and Brandenburg R 2017 *Plasma Sources Sci. Technol.* **26** 123002
[4] Bílek P, Kuthanová L, Hoder T and Šimek M 2022 *Plasma Sources Sci. Technol.* **31** 084004
[5] Li J, Lei B, Wang J, Xu B, Ran S, Wang Y, Zhang T, Tang J, Zhao W and Duan Y 2021 *Commun. Phys.* **4** 64
[6] Massines F, Rabehi A, Decomps P, Gadri R B, Ségur P, Mayoux C, Rami B G and Sé P 1998 *J. Appl. Phys.* **83** 2950
[7] Massines F, Gherardi N, Naudé N and Ségur P 2009 *Eur. Phys. J. Appl. Phys.* **47** 22805
[8] Zhu Y, Starikovskaia S M, Babaeva N Y and Kushner M J 2020 *Plasma Sources Sci. Technol.* **29** 125006
[9] Bischoff L *et al* 2018 *Plasma Sources Sci. Technol.* **27** 125009
[10] Balcon N, Hagelaar G and Boeuf J 2008 *IEEE Trans. Plasma Sci.* **36** 2782–7
[11] Robert R, Hagelaar G, Sadeghi N, Stafford L and Massines F 2024 *J. Appl. Phys.* **135** 153303
[12] Liu Y *et al* 2023 *Plasma Sources Sci. Technol.* **32** 025012
[13] Schulze J, Schüngel E, Donkó Z and Czarnetzki U 2011 *Plasma Sources Sci. Technol.* **20** 015017
[14] Gans T, Schulze J, O'Connell D, Czarnetzki U, Faulkner R, Ellingboe A R and Turner M M 2006 *Appl. Phys. Lett.* **89** 261502
[15] Korolov I, Donkó Z, Hübner G, Liu Y, Mussenbrock T and Schulze J 2021 *Plasma Sources Sci. Technol.* **30** 095013
[16] Bazinette R, Sadeghi N and Massines F 2020 *Plasma Sources Sci. Technol.* **29** 095010
[17] Magnan R, Hagelaar G, Chaker M and Massines F O 2020 *Plasma Sources Sci. Technol.* **29** 035009
[18] Magnan R, Hagelaar G, Chaker M and Massines F 2021 *Plasma Sources Sci. Technol.* **30** 015010
[19] Robert R, Hagelaar G, Sadeghi N, Magnan R, Stafford L and Massines F 2022 *Plasma Sources Sci. Technol.* **31** 065010
[20] Zhou Y J, Yuan Q H, Li F, Wang X M, Yin G Q and Dong C Z 2013 *Phys. Plasmas* **20** 113502
[21] Patelli A, Verga E, Nodari L, Petrillo S, Delva A, Ugo P and Scopece P 2018 A customised atmospheric pressure plasma jet for conservation requirements *IOP Conf. Ser.: Mater. Sci. Eng.* **364** 012079
[22] You S, Patelli A, Ghamgosar P, Cesca T, Enrichi F, Mattei G and Vomiero A 2019 *APL Mater.* **7** 081111
[23] Habib T, Ceroni L, Patelli A, Caiut J M A and Caillier B 2023 *Plasma* **6** 623–36
[24] Maffei A *et al* 2020 *Appl. Surf. Sci.* **507** 144713
[25] Patelli A, Mussano F, Brun P, Genova T, Ambrosi E, Michieli N, Mattei G, Scopece P and Moroni L 2018 *ACS Appl. Mater. Interfaces* **10** 39512–23
[26] Patelli A, Verga Falzacappa E, Scopece P, Pierobon R and Vezzù S 2017 *Method for generating an atmospheric plasma jet and atmospheric plasma minitorch device United States* US9693441B2 (available at: https://patents.google.com/patent/US9693441)
[27] Heirman P, Van Boxem W and Bogaerts A 2019 *Phys. Chem. Chem. Phys.* **21** 12881–94
[28] Gaens W V and Bogaerts A 2013 *J. Phys. D: Appl. Phys.* **46** 275201
[29] Iseni S, Zhang S, Van Gessel A F, Hofmann S, Van Ham B T, Reuter S, Weltmann K D and Bruggeman P J 2014 *New J. Phys.* **16** 123011
[30] Zhang S, Sobota A, Van Veldhuizen E M and Bruggeman P J 2015 *J. Phys. D: Appl. Phys.* **48** 095401
[31] Yamabe C, Buckman S J and Phelps A V 1983 *Phys. Rev.* A **27** 1345–52
[32] Zatsarinny O and Bartschat K 2004 *J. Phys. B: At. Mol. Opt. Phys.* **37** 4693–706
[33] Hayashi M 2003 Bibliography of electron and photon cross sections with atoms and molecules published in the 20th century *Argon Technical Report* NIFS-DATA-72 (National Institute for Fusion Science (NIFS) of Japan Toki (Japan))
[34] Eletskii A V and Smirnov B M 1986 *J. Sov. Laser Res.* **7** 207–323
[35] Rapp D and Briglia D D 1965 *J. Chem. Phys.* **43** 1480–9
[36] Flannery M and McCann K J 1980 Cross sections for ionization of rare gas excimers by electron impact and atomic and molecular processes in excimer lasers *Technical Report* (AFWAL-TR-80-2015 Georgia Institute of Technology Atlanta (USA))
[37] Jones J D C, Lister D G, Wareing D P and Twiddy N D 1980 *J. Phys. B: At. Mol. Phys.* **13** 3247–55
[38] Kolokolov N B, Kudrjavtsev A A and Blagoev A B 1994 *Phys. Scr.* **50** 371–402
[39] Lukáč P, Mikuš O, Morva I, Zábudlá Z, Trnovec J and Morvová M 2011 *Plasma Sources Sci. Technol.* **20** 055012
[40] Biondi M A 1974 Recombination *Principles of Laser Plasmas* 1st edn, ed G Bekefi (Wiley) pp 125–58
[41] Millet P, Birot A, Brunet H, Dijolis H, Galy J and Salamero Y 1982 *J. Phys. B: At. Mol. Phys.* **15** 2935–44
[42] Irimia A and Fischer C F 2004 *J. Phys. B: At. Mol. Opt. Phys.* **37** 1659–72
[43] Wiese W L, Brault J W, Danzmann K, Helbig V and Kock M 1989 *Phys. Rev.* A **39** 2461–71
[44] Stankov M, Becker M M, Hoder T and Loffhagen D 2022 *Plasma Sources Sci. Technol.* **31** 125002
[45] Sigeneger F, Becker M M, Foest R and Loffhagen D 2016 *J. Phys. D: Appl. Phys.* **49** 345202
[46] Bogaerts A and Gijbels R 1999 *J. Appl. Phys.* **86** 4124–33
[47] Ellis H, Thackston M, McDaniel E and Mason E 1984 *At. Data Nucl. Data Tables* **31** 113–51
[48] Phelps A V 1991 *J. Phys. Chem. Ref. Data* **20** 557–73
[49] Phelps A V and Petrovic Z L 1999 *Plasma Sources Sci. Technol.* **8** R21–R44
[50] Taghizadeh L, Van Der Mullen J, Nikiforov A and Leys C 2015 *Plasma Process. Polymers* **12** 799–807

[51] Yanguas-Gil A, Focke K, Benedikt J and Von Keudell A 2007 *J. Appl. Phys.* **101** 103307
[52] Nikiforov A Y, Leys C, Gonzalez M A and Walsh J L 2015 *Plasma Sources Sci. Technol.* **24** 34001
[53] Moon S Y, Rhee J K, Kim D B and Choe W 2006 *Phys. Plasmas* **13** 033502
[54] Cámara-Torres M, Sinha R, Scopece P, Neubert T, Lachmann K, Patelli A, Mota C and Moroni L 2021 *ACS App. Mater. Interfaces* **13** 3631–44
[55] Filice D and Coulombe S 2024 *Plasma Sources Sci. Technol.* **33** 055011
[56] Vanraes P and Bogaerts A 2021 *J. Appl. Phys.* **129** 220901